Nuclear Science and Techniques (2024) 35:10
https://doi.org/10.1007/s41365-024-01381-w

Generation and regulation of electromagnetic pulses generated by femtosecond lasers interacting with multitargets

Ya-Dong Xia[1,2] · De-Feng Kong[1,2] · Qiang-You He[1,2] · Zhen Guo[1,2] · Dong-Jun Zhang[4] · Tong Yang[1,2] · Hao Cheng[1,2] · Yu-Ze Li[1,2] · Yang Yan[1,2] · Xiao Liang[4] · Ping Zhu[4] · Xing-Long Xie[4] · Jian-Qiang Zhu[4] · Ting-Shuai Li[5] · Chen Lin[1,2,3] · Wen-Jun Ma[1,2,3] · Xue-Qing Yan[1,2,3]

Received: 30 June 2023 / Revised: 24 November 2023 / Accepted: 29 November 2023 / Published online: 29 January 2024
© The Author(s), under exclusive licence to China Science Publishing & Media Ltd. (Science Press), Shanghai Institute of Applied Physics, the Chinese Academy of Sciences, Chinese Nuclear Society 2024

Abstract

Ultrashort and powerful laser interactions with a target generate intense wideband electromagnetic pulses (EMPs). In this study, we report EMPs generated by the interactions between petawatt (30 fs, 1.4×10^{20} W/cm^2) femtosecond (fs) lasers with metal flat, plastic flat, and plastic nanowire-array (NWA) targets. Detailed analyses are conducted on the EMPs in terms of their spatial distribution, time and frequency domains, radiation energy, and protection. The results indicate that EMPs from metal targets exhibit larger amplitudes at varying angles than those generated by other types of targets and are enhanced significantly for NWA targets. Using a plastic target holder and increasing the laser focal spot can significantly decrease the radiation energy of the EMPs. Moreover, the composite shielding materials indicate an effective shielding effect against EMPs. The simulation results show that the NWA targets exert a collimating effect on thermal electrons, which directly affects the distribution of EMPs. This study provides guidance for regulating EMPs by controlling the laser focal spot, target parameters, and target rod material and is beneficial for electromagnetic-shielding design.

Keywords Electromagnetic pulses · Laser plasma interaction · Electromagnetic shielding · Electron distribution

This work was supported by the National Natural Science Foundation of China (Nos. 12122501, 11975037, 61631001, and 11921006), the National Grand Instrument Project (Nos. 2019YFF01014400, 2019YFF01014404), and the Foundation of Science and Technology on Plasma Physics Laboratory (No. 6142A04220108).

✉ Chen Lin
lc0812@pku.edu.cn

✉ Wen-Jun Ma
wenjun.ma@pku.edu.cn

1 State Key Laboratory of Nuclear Physics and Technology, and Key Laboratory of HEDP of the Ministry of Education, CAPT, Peking University, Beijing 100871, China

2 Beijing Laser Acceleration Innovation Center, Beijing 101407, China

3 Institute of Guangdong Laser Plasma Technology, Guangzhou 510540, China

4 National Laboratory on High Power Laser and Physics, Shanghai Institute of Optics and Fine, Chinese Academy of Sciences, Shanghai 201800, China

5 School of Materials and Energy, University of Electronic Science and Technology of China, Chengdu 611731, China

1 Introduction

Laser-matter interactions can result in extremely complex physical processes. Under diverse experimental conditions, such as different laser and plasma parameters, the mechanism of energy-absorbing laser energy may differ significantly owing to the combined action of several mechanisms, including collision absorption [1], resonance absorption [2], vacuum heating [3], J×B heating [4], and laser wakefield acceleration [5]. These mechanisms result in the complex motion of hot electrons, which is applicable to many areas, such as fast ignition [6, 7], free-electron lasers [8], bremsstrahlung radiation sources [9, 10], and medical isotope production [11]. According to electromagnetic field and electrodynamic theories, this motion of hot electrons induces intricate time-varying electromagnetic fields.

Researchers showed that for laser-matter interactions, the radiation intensities of electromagnetic pulses (EMPs) generated exceed several hundred kilovolts per meter [12–14], the bandwidth is dozens of megahertz to ~5 GHz [15–19], and the duration is on the order of hundreds of nanoseconds.

Because this frequency range is the primary cause of electronic component damage, it can result in malfunction or even damage to electronic equipment in or near the target chamber. The mechanism of EMPs generated by laser interaction with a solid target is primarily derived from hot electrons [18], neutralization currents [20], secondary hot electrons [21], and other particles emitted from plasma [22].

As laser-matter interactions can result in extremely complex physical processes, radiated EMPs are directly or indirectly affected by various experimental conditions. Therefore, the effects of the laser, target, and target holder parameters on radiated EMPs have been investigated extensively. Varma et al. [23] discovered that by using a nanosecond laser as a pre-pulse and then allowing it to interact with glass and copper targets through femtosecond (fs) lasers, the EMPs increased by several orders of magnitude. Bradford et al. [24] proposed the idea of controlling EMPs via the energy and duration of laser, the structure and material of the target holder, and the pre-pulse delay. Nelissen et al. [25] investigated the functional relationship between the radiation strengths of EMPs and the intensity and energy of laser on a 200 TW fs laser device in the Centro de Laseres Pulsados (CLPU) laser center. Brown et al. [26] discovered a positive correlation between the number of emitted hot electrons and each of the intensity of EMPs and the target size. Jinwen Yang et al. [12] and Ming Yang et al. [13] measured and analyzed the characteristics of EMPs generated by the interaction of an intense laser with different targets and discovered that the time-domain waveforms of the EMPs were diverse. In the Compact Laser Plasma Accelerator, we observed that pre-plasma was successfully generated by subjecting a target to a 200 ps pre-ablative laser, which caused both the protons and EMPs to improve significantly [27]. Basic investigations pertaining to laser continue to increase worldwide, and laser devices are being developed toward the petawatt and exawatt classes [28, 29]. Consequently, the issue of EMP interference will become increasingly severe, thus indicating that the characteristics and shielding protection against this radiation are crucial. In 2020, Consoli et al. [30] published a comprehensive review article that summarizes the research findings and challenges encountered in recent years in international large-scale facility laboratories regarding the generation mechanisms, influencing factors, detection results, and mitigation methods of EMPs in the context of the interaction between high-power, high-energy laser pulses and various types of targets. Previous studies have established a basis for understanding the EMP mechanism and the effects of experimental variables on EMP radiation.

In this paper, we summarized the experimental measurement results of a Shenguang-II petawatt (PW) laser device. We focus on investigating the spatial distribution, time and frequency domains, and radiation energy of EMPs generated by interactions between a PW laser and each of aluminum (Al) flat, plastic flat, and plastic nanowire-array (NWA) targets, among which the generation of EMP from NWA targets is investigated for the first time. NWA targets involve the addition of nanostructures to the target surface to enhance laser absorption and optimize the conditions for producing high-density thermal materials. These nanostructures change the emission direction of thermal electrons and the EMP radiation. Therefore, accurate information regarding the spatial distribution of the radiation of different targets must be obtained. Unlike these previous studies, we employ a sufficient number of antennas to comprehensively measure the spatial distribution of EMPs inside and outside the target chamber.

The findings reveal that among the three different targets, the Al targets generate the most EMPs because of their abundance of free-moving electrons, and the spatial distribution of their signals is more uniform. The NWA targets significantly improve the EMPs, and the peak emission angle changes toward the laser direction, owing to the fact that the NWA targets can promote energy conversion efficiency and generate more collimated thermal electrons. Additionally, we discovered that the characteristics of EMPs are closely related to the target holder materials and laser focal spot size. Section 3 provides a detailed comparison and analysis of the results. Additionally, we investigate the effect of EMP attenuation on the thickness of the shielding composite materials in a PW laser device and discovered a positive correlation between them. This study serves as a valuable reference for understanding the features of EMPs generated by high-energy fs lasers interacting with targets under different conditions and suggests valuable methods for electromagnetic shielding.

2 Experiment arrangement

A PW laser experiment was performed at the Shenguang-II (SG-II) Multi-Petawatt Laser facility [31, 32] at the National Laboratory on High Power Laser and Physics, Shanghai Institute of Optics and Fine Mechanics. The experimental setup is illustrated in Fig. 1. The laser with effective energy to the target (30 fs, 21 J) interacted with Al flat and polyethylene targets, including carbon-deuterium (CD) flat, carbon-deuterium nanowire-array (CDNWA) targets, for 12 shots, as shown in Table 1. For shots no. 3 and nos. 6–8, plastic holders (PHs) were used, whereas metal holders (MHs) were used for the other shots. The targets used in the experiment were circular, with a diameter of 2 mm. The length of the target holder (fabricated using Al or carbon-hydrogen (CH) polymer) was 30 mm. The incidence angle of the laser was 25° with respect to the target's normal direction. The laser exhibited full width at half maximum (FWHM) values of 22, 30, 40, and 107 μm, an energy density of approximately

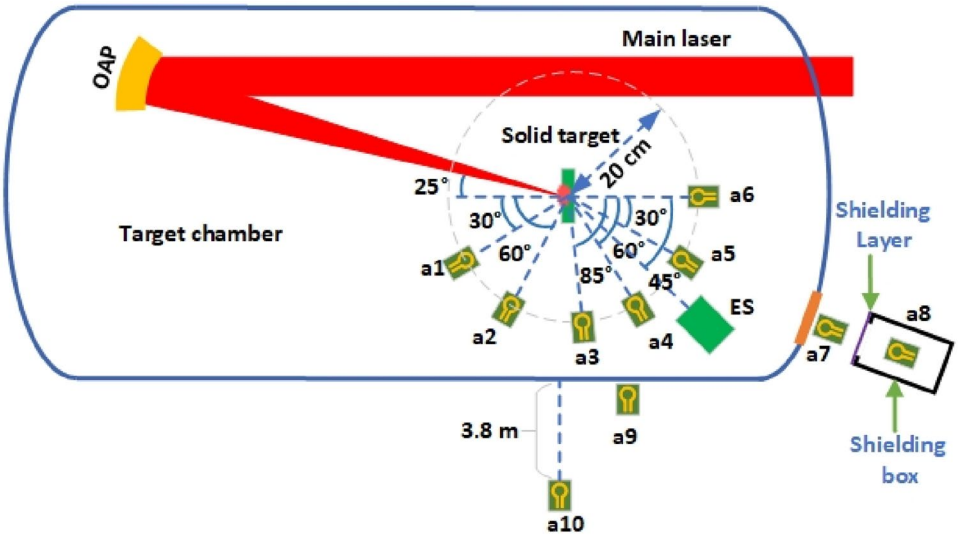

Fig. 1 (Color online) Schematic illustration of experimental arrangement for SG-II PW laser device

Table 1 Parameters of targets, focal spots, and diagnostic equipment used in current experiment

No	Target	Thickness	FWHM	Diagnostic device
1	Al flat (MH)	10 μm	22 μm	a1–a8
2	CD flat (MH)	450 μm	22 μm	a1–a8
3	CD flat (PH)	450 μm	22 μm	a1–a8
4–5	CDNWA (MH)	450 μm + 8 μm (± 3 μm)	22 μm	a1–a8
6–8	CDNWA (PH)	450 μm + 8 μm (± 3 μm)	22 μm	a1–a8
9	CDNWA (MH)	450 μm + 8 μm (± 3 μm)	22 μm	a5, a7–a10, ES
10	CDNWA (MH)	450 μm + 8 μm (± 3 μm)	30 μm	a5, a7–a10, ES
11	CDNWA (MH)	450 μm + 8 μm (± 3 μm)	40 μm	a5, a7–a10, ES
12	CDNWA (MH)	450 μm + 8 μm (± 3 μm)	107 μm	a5, a7–a10, ES

Al flat and CD flat, CDNWA targets with MHs and PHs were used. Thickness of CDNWA represents 450 μm CD flat + 8 μm long nanoarrays. Focal spot sizes were 22, 30, 40, and 107 μm. Diagnostic devices contain a1–a10 B-dots and ES; shots nos. 1–8 use a1–a8 B-dots, whereas shots nos. 9–12 use a5, a7–a10, and ES

1.4×10^{20} W/cm^2, and a contrast of 10^8 at approximately 100 ps.

In the target chamber, six SGIIIB01-2 small B-dot antennas [33] (a1–a6) were mounted at various angles, with the target point positioned at the center and a radius of 20 cm. Antennas a1 and a2 were positioned in front of the target at angles of 30° and 60°, respectively, in a direction normal to the target. Antennas a3, a4, a5, and a6 were positioned behind the target at angles of 85°, 60°, 30°, and 0°, respectively. Four additional B-dot antennas, a7–a10, were placed outside the target chamber. Specifically, a7 was mounted on the glass flange; a8 was placed inside the shield box; a9 was positioned on the metal flange; and a10 was positioned 3.8 m away from the target chamber wall, i.e., 4.2 m away from the target center. Table 2 presents a visual representation of the antenna locations. In terms of the antenna-to-oscilloscope connection, each B-dot antenna was first connected to an RF coaxial cable with double shielding and then transferred to the outside through the flange; finally, the cable and various

Table 2 Specific location of diagnostic antenna and electron spectrometer

Spatial position	No. of B-dot	Angle with the target normal direction	Distance from target center
Front of target	a1	30°	20 cm
	a2	60°	20 cm
Back of target	a3	85°	20 cm
	a4	60°	20 cm
	a5	30°	20 cm
	a6	0°	20 cm
Outside of chamber	a7	35°	65 cm
	a8	35°	75 cm
	a9	70°	40 cm
	a10	90°	4.2 m

attenuators were connected sequentially to a 13 GHz bandwidth oscilloscope to measure the EMPs. The time-domain signals of the EMPs can be calculated by multiplying the oscilloscope signals and attenuations. A calibrated electron spectrometer (ES) with a magnetic field of 500 G was placed 45° and 30 cm behind the target and used to monitor the escaped hot electrons. The shielding box was a 166 mm cube constructed using 3-mm-thick permalloy. A circular window with a diameter of 110 mm was cut on one side of the box, and a composite shielding material was placed on this opening. The shielding effectiveness of the material was evaluated by measuring the EMP inside and outside the shielding box.

3 Results and discussion

3.1 EMP distribution in target chamber

Figure 2 shows the variations in the distributions of the EMP peak amplitudes obtained by calculating the maximum absolute value of the signal amplitude in the time domain. These EMPs were generated by the interaction between the PW laser and different targets, including the Al flat (MH), CD flat (MH), CD flat (PH), CDNWA (MH), and CDNWA (PH) targets. The result indicate that the EMP distributions were affected significantly by the spatial position: (1) For the Al target, the peak value was significantly higher and the distribution was more uniform at diverse angles compared with those of the other targets. (2) The EMP intensities of the CD and CDNWA targets using PHs were significantly lower than those using MHs. This is expected as the MH has a higher conductivity than the PH, which implies that it can generate a larger return current under similar shooting conditions [24]. (3) In front of the target, the overall distributions from the CD and CDNWA were uneven and stronger along the laser reflection direction a1. (4) At the back of the target, the CD and Al targets exhibited the strongest signal along the a4 position, whereas for the CDNWA targets with improved EMP performance compared with regular planar targets, the strongest signal was observed along a5, which was the closest to the transmission direction of the laser. Several studies showed that NWA targets can improve laser absorption and plasma-conversion efficiency compared with ordinary solid targets [34–37]. For the NWA targets, approximately 50% of the energy can be converted into electrons [38], which subsequently enhances the radiated EMPs [27, 39]. (5) Additionally, we observed that the peak values of the five targets were higher at the back of the target than in front of the target, which is consistent with the emission direction of the high-energy-density electrons.

3.2 Results in time and frequency domains

To investigate the variations in the time and frequency domains as well as the energy of EMPs generated by the interaction of the PW laser with the Al flat (MH), CD flat (MH), CD flat (PH), CDNWA (MH), and CDNWA (PH) targets, five EMP signals from the a5 antenna were compared. Here, "0 ns" refers to the time at which the laser interacts with the target. Figure 3 shows the peak intensities of the EMPs based on the Al flat (MH), CD flat (MH), CD flat

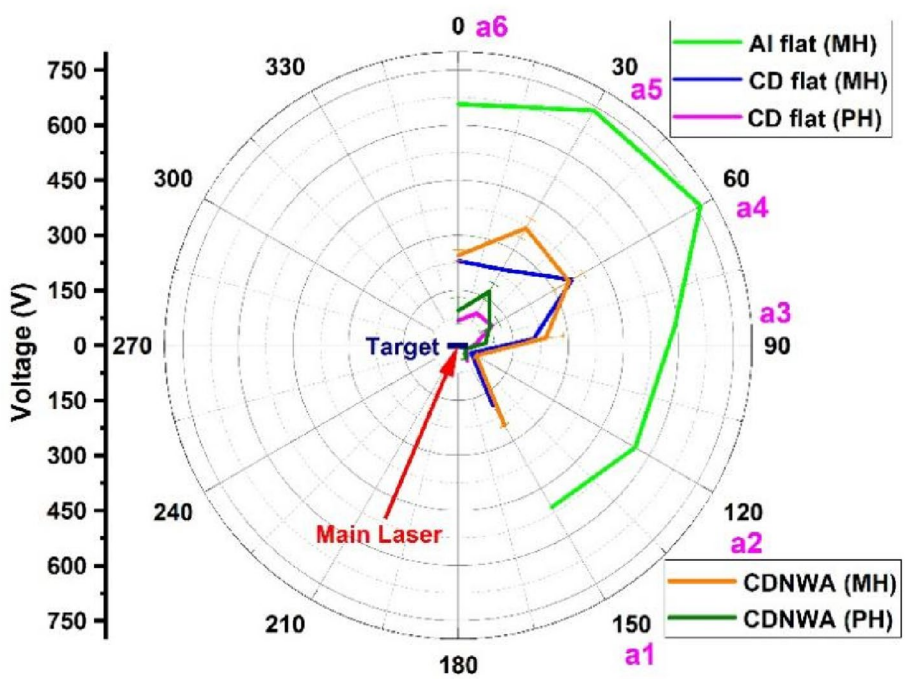

Fig. 2 (Color online) Distribution of peak of EMPs generated by PW laser collision with different targets, including Al flat (MH), CD flat (MH), CD flat (PH), CDNWA (MH) and CDNWA (PH) targets; measurement was performed at a1 to a6 from different angles with respect to normal direction of target. Red arrow indicates incident direction of laser, which is 25° relative to the normal direction of the target; and all laser focal spots measure 22 μm

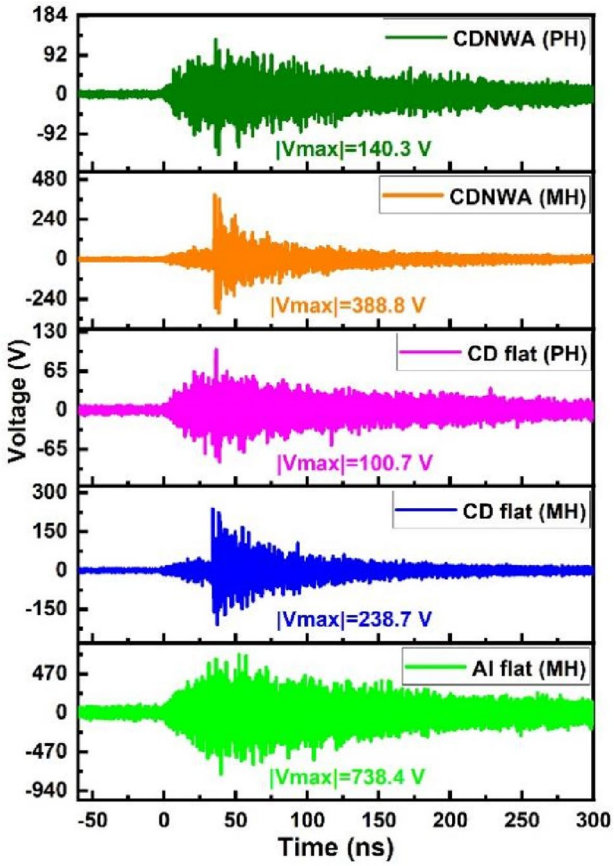

Fig. 3 (Color online) Time domains of five EMPs generated by PW laser interacting with Al flat (MH), CD flat (MH), CD flat (PH), CDNWA (MH) and CDNWA (PH) targets at position a5

(PH), CDNWA (MH), and CDNWA (PH) targets, whose intensities were 738.4, 238.7, 100.7, 388.8, and 140.3 V, respectively. The results indicate that the EMPs generated by the laser-target interactions depended on the material properties of the target (the greatest for metal, followed by the CDNWA and CD) and the target holder (metal larger than plastic). Notably, the EMP magnitude increased at 34 ns for both the CDNWA (MH) and CD flat (MH) targets. The CDNWA (MH), CD flat (MH), CDNWA (PH), CD flat (PH), and AL flat (MH) targets differ in terms of the material combinations used for the target rod and body. Specifically, the first two incorporate a combination of insulators and conductors, whereas the last three involve combinations of similar materials, i.e., insulators with insulators or conductors with conductors.

For the insulator-conductor combinations, once the threshold voltage (known as the insulator breakdown voltage) is surpassed, the resistance to electron movement decreases significantly. During the interaction between the laser and target, significant electron emission from the target increases the potential difference. Electrons from the target rod, which are connected to the ground, compensate for the missing electrons. In the initial phase, the potential difference is amplified because the electron supply is not compensated timely. Once the breakdown voltage is breached, the electrons rush in swiftly, thus significantly increasing the return current. Because this current is one of the primary sources of EMPs, the observed signal is diminished significantly.

The observed trends of the curve suggest that the EMP attenuation is slower and persists for a longer duration when an Al target or plastic target rod is used. In particular, the curve exhibits a gradual decay over an extended period when compared with other target materials, thus indicating that the EMP attenuation properties of these materials differ significantly.

To gain a more comprehensive understanding of the temporal and spectral properties of EMPs, we employed wavelet transform to analyze the signals depicted in Fig. 3; the resulting time-frequency diagram is presented in Fig. 4. For the Al flat (MH) target, when the laser reached the target, the EMP energy was primarily released within 0–120 ns, with the spectral concentration primarily in the higher frequency range between 14 and 16 GHz, along with higher harmonic oscillations at 7 and 14 GHz. The high-order harmonics were generated owing to nonlinear effects. For example, during the interaction between the laser and target, the generated EMPs were generated via multiple mechanisms, thus resulting in a rich frequency spectrum. Throughout the propagation of the EMPs, these frequencies underwent superposition, mixing, reflection, and other effects, thus resulting in nonlinear responses. Meanwhile, the free-electron density of the target material changed significantly, which induced thermal effects in the target and resulted in plasmas with varied density distributions. When an EMP propagates and encounters these media or interfaces, the nonlinear effects result in new frequency components with high-order harmonics. Additionally, a few EMPs continued to radiate between 120 and 260 ns. The EMPs generated by the CD flat (PH) and CDNWA (PH) targets exhibited similar durations and frequencies as the Al (MH) target, albeit with different intensities.

An analysis of the CD flat (MH) and CDNWA (MH) targets revealed that, compared with the case of other targets, the EMPs generated by these targets were primarily dispersed in a lower frequency range and had a relatively short duration of approximately 100 ns following the arrival of the primary laser pulse at the target. The specific energy distribution and frequency characteristics of the EMPs are shown in Fig. 5.

To analyze the frequency components of the signals depicted in Fig. 3, we performed the fast Fourier transform to convert the time-domain signals into frequency-domain amplitudes. Subsequently, we squared and divided the

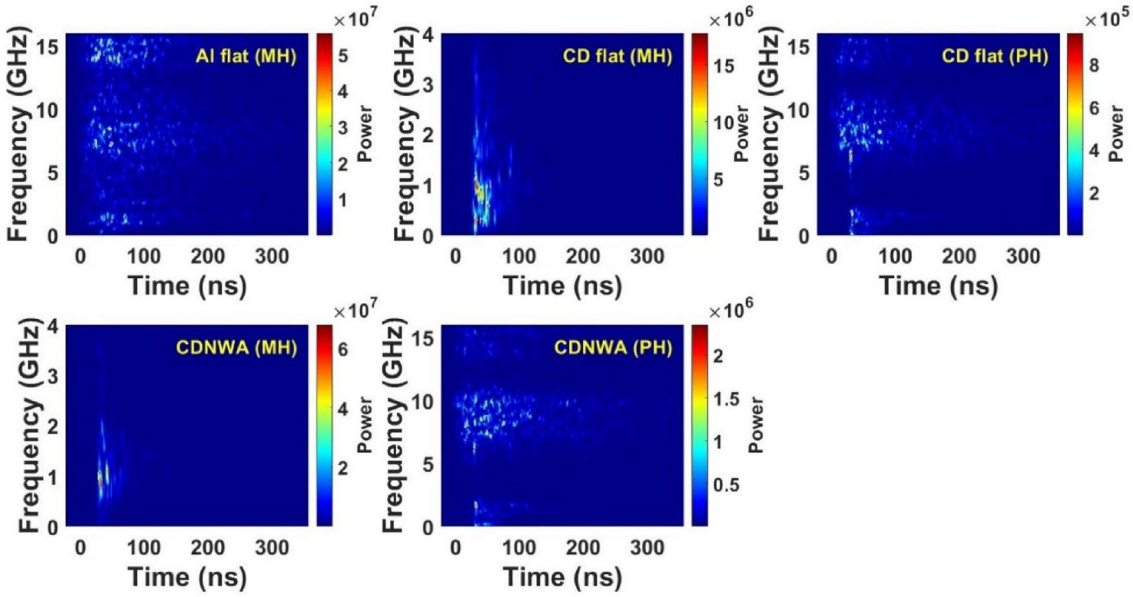

Fig. 4 (Color online) Relationship between time and frequency obtained via wavelet transformation of signals presented in Fig. 3

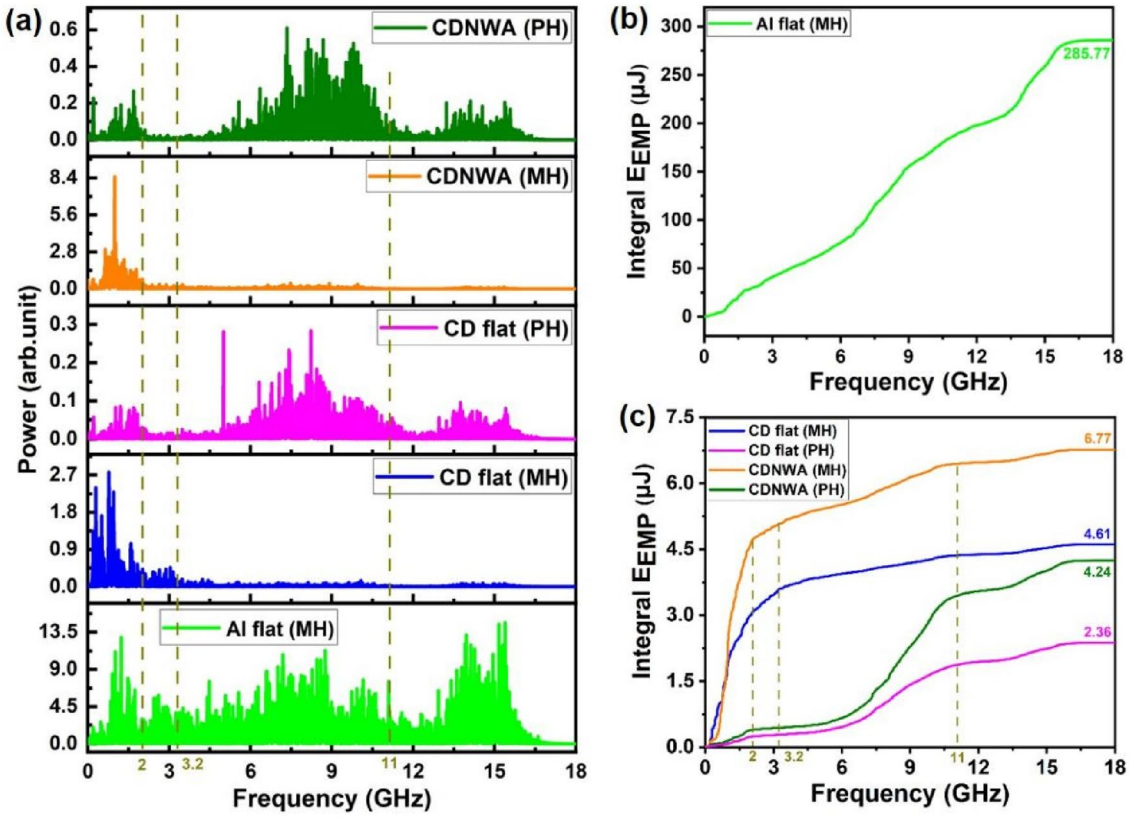

Fig. 5 (Color online) **a** Power spectra of signals from Fig. 3; **b** total integrated energy of Al target from (**a**); **c** total integrated energy of other four targets. Spectra complexity is attributable to various factors, including multiple possible sources of EMPs and internal arrangement of target chamber, as discussed in prior publications [30, 40, 41]

spectra by 2 to obtain the power spectra. The resulting power spectra are illustrated in Fig. 5a, which show the spectral properties of the EMPs generated by the interaction of the PW laser with the Al flat (MH), CD flat (MH), CD flat (PH), CDNWA (MH), and CDNWA (PH) targets.

As shown in Fig. 2, the distribution of EMPs is non-uniform, thus rendering the formula for uniform distribution [27] inadequate for evaluating the power radiated by the EMPs. Hence, we incorporated a distribution coefficient β into the original formula, which yielded a more precise evaluation of the radiated power. β considers the non-uniform distribution of EMPs and is derived by averaging the ratio of EMP peak values between a1–a6 and a5. The total integrated energy of the EMPs (E_{EMP}) can be evaluated using Eq. (1).

$$E = \frac{\beta \times \left(2\pi d^2 P\right) \times \tau_{\mathrm{EMP}}}{\pi r^2 \times R}, \tag{1}$$

where P is the radiant power obtained by integrating the power spectra shown in Fig. 5a. The distance from the antenna to the target is $d = 20$ cm and the effective radius of B-dot is $r = 0.5$ cm. The EMP duration τ_{EMP} is 260 ns for the Al flat (MH), CD flat (PH), and CDNWA (PH) targets, and 100 ns for the CD flat (MH) and CDNWA (MH) targets. The load resistance R is 50 Ω. The distribution coefficients β for the targets above are 0.86, 0.88, 0.65, 0.71, and 0.49, respectively. The E_{EMP}, as shown in Fig. 5b and c, indicates that the total integrated energy of the Al flat (MH), CD flat (MH), CD flat (PH), CDNWA (MH), and CDNWA (PH) targets are 285.77, 4.61, 2.36, 6.77, and 4.24 μJ, respectively. An early study [24] showed that using PHs reduced the energy of EMPs by 1/3 compared with using MHs. Our test results indicated a similar trend: The EMP energy based on CD flat (PH) was 0.52 times that of CD flat (MH), whereas the EMP energy of CDNWA (PH) was 0.79 times that of CDNWA (MH).

The power spectral distribution can be observed more clearly from the increasing trend of the integrated energy. First, the Al flat (MH) target demonstrated the widest and strongest energy distribution, which primarily dispersed within the range of 0–16 GHz. Second, the EMPs generated from the CDNWA (MH) target were primarily distributed below 2 GHz, with a narrow power range between 2 and 11 GHz and a shorter power range from 11 to 16 GHz. Third, the CD flat (PH) and CDNWA (PH) targets primarily appeared in the range of 6 to 11 GHz, and the CD flat (MH) target was distributed below 3.2 GHz.

The results of the power spectra and integral energy indicated strong dependence on the type of target and target holder used. Specifically, (1) the EMP radiation energy from the NWA target was, on average, 1.6 times higher than that from a typical plastic target. However, this increase in energy was only evident in the amplitude of the spectrum, whereas no clear changes were observed in the spectral range. (2) The EMP generated by the metal target rod was, on average, 1.8 times larger than that generated by the plastic target rod. Nevertheless, the energy values in the frequency ranges of 0–2 GHz and 2–16 GHz indicated that the low-frequency region of the EMP spectrum was suppressed, whereas the high-frequency region was enhanced when the plastic target rod was used. (3) The EMPs generated by the metal targets exhibited a significantly higher energy, i.e., approximately 62 times greater than that generated by the plastic targets. Furthermore, the spectra of these EMPs were the widest and strongest, thus resulting in to severe interference with electronic equipment. This phenomenon is due to the metal targets generating more energetic hot electrons and the low resistivity of the metal, thus promoting the lateral transport of the electrons. If these energetic electrons exhibit higher acceleration rates, escape velocities, and quantities, then EMPs with higher frequencies and greater power can be generated [27]. In addition, the neutralization current predominantly radiated strong EMPs at low frequencies, which is similar to the result presented in a previous study [42].

3.3 EMPs and hot electrons in different focal spots

Figure 6 shows the EMP radiation energy and thermal electron energy spectra measured by the ES, as shown in Fig. 1, for four different focal spots. The total EMP energies yielded by the interaction between the PW laser and CDNWA (MH) target for focal spots of 22, 30, 40, and 107 μm were 6.77, 2.31, 0.4, and 0.31 μJ, respectively. The exponential fitting of the normalized total E_{EMP} (y_1) and the focal spot size (x) showed an exponentially decaying relationship expressed by the function $y_1 = 25.65 \times e^{(-x/6.73)} + 0.03$. The normalized total N_e (y_2) decreased as the focal spot size increased [i.e., $y_2 = 5.15 \times e^{(-x/10.78)} + 0.33$], which indicates a similar trend between the intensity of EMPs and the number of hot electrons with varying focal spot sizes, thus further emphasizing that hot electrons are one of the primary sources contributing to EMPs. Additionally, the results suggest the potential of controlling the EMP radiation energy and the number of hot electrons by adjusting the focal spot of the laser, which offers valuable insights into the investigation and application of EMPs in various fields.

3.4 Simulation result discussion

We employed the two-dimensional PIC software EPOCH to simulate thermal electron emission from three targets. The simulation box measured 40 μm × 20 μm and comprised a 4000 × 2000 grid, with each grid containing 30 superparticles. The spatial resolution was 10 nm × 10 nm. A linearly polarized 800 nm laser beam with a pulse width of 10 laser cycles and an FWHM of 4.3 μm was utilized; it was incident

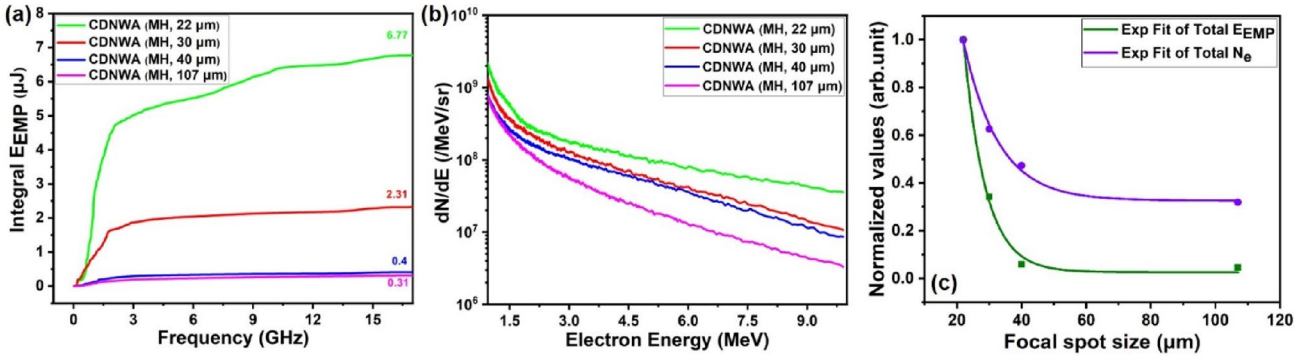

Fig. 6 (Color online) **a** Total integrated energy of CDNWA (MH) target from four different focal spots measuring 22, 30, 40, and 107 μm; **b** electron spectroscopy results for the four spots; **c** two exponential fits among total number of hot electrons (N_e), total energy of EMP (E_{EMP}) and focal spot size, where N_e and E_{EMP} are normalized with their respective highest values

on the targets at an angle of 25° with respect to the target normal. The focal spot was located between −1 and −7 μm on the vertical axis in the figure, with a peak intensity of 1×10^{20} W/cm^2. Three different targets were utilized in the simulation: carbon-hydrogen nanowire-array (CHNWA), CH, and Al targets, whose thicknesses were 10, 10, and 4 μm, respectively. The atomic number densities of C/Al were 37.5, 37.5, and 35 n_c, where $n_c = 1.7\times10^{21}$ cm^{-3} represents the critical plasma density for an 800 nm laser. The initial ionization conditions were C^{2+}, H^+, and Al^{9+} for the CHNWA, CH, and Al targets, respectively. Additionally, we considered the effect of pre-pulses on the targets. The pre-plasma distribution for all targets can be expressed as shown in Eq. (2):

$$n = n_0 e^{\frac{-\Delta x}{L}}, \tag{2}$$

where the ionized particles for the CHNWA and CH targets is H^+, and Al^{9+} for Al. Here, n_0 represents the initial atom number density; L is the plasma scale length, which is 0.16 μm; and Δx is the distance from the target surface. A similar simulation method was used in previous studies [43, 44].

A graphical representation of our findings is presented in Fig. 7, where (a–c) show the electron densities of the Al,

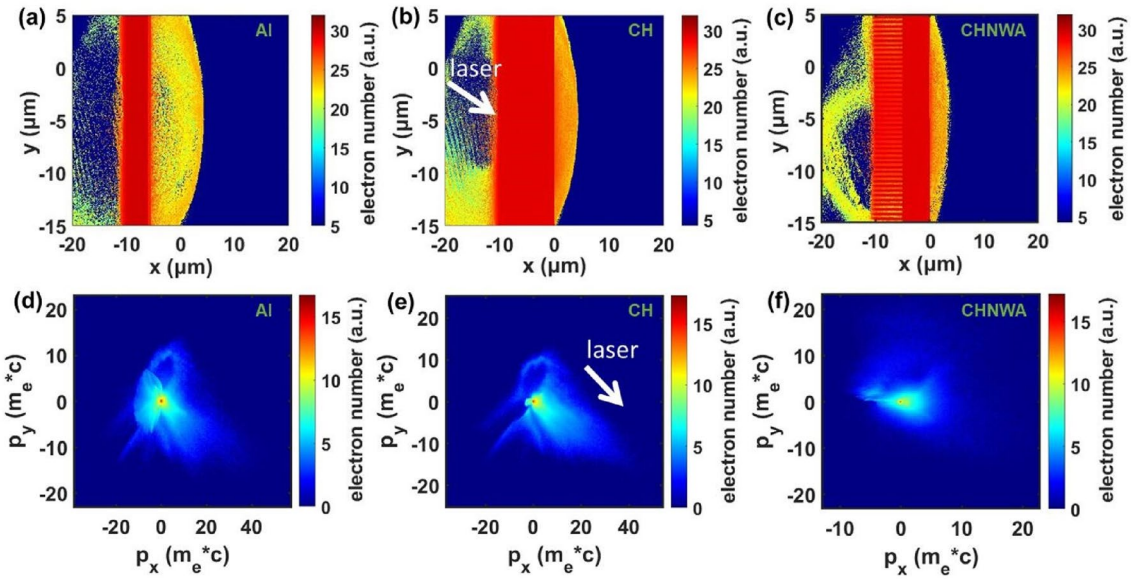

Fig. 7 (Color online) **a**–**c** Density distributions of hot electrons generated by interaction between laser and Al flat, CH flat, and CHNWA targets. **d**–**f** Space momentum distribution of hot electrons for three targets. Laser incidence occurred at $t = 0$ and reached target surface at $t = 27$ fs, whereas electron distribution presented in simulation results is relevant to $t = 133$ fs

CH, and CHNWA targets, respectively, at a simulation time of $t = 133$ fs, and (d–f) show the corresponding momentum space distribution of electrons at the same simulation time. The results show a relatively uniform distribution for the Al target, which is consistent with the insignificant distribution difference of the EMP shown in Fig. 2. Comparatively, the CH target tended to propagate toward the rear side of the target in the direction of laser propagation. During the interaction between the laser and NWA targets, the self-generated electromagnetic field exhibited the behavior of a lens, i.e., it confined and trapped hot electrons between the nanowires. This reduced the scattering and diffusion of hot electrons, thus enabling them to acquire relativistic energy via a direct laser-acceleration mechanism [45, 46]. Therefore, the microstructure of the NWA targets results in the collimation of hot electrons, thus causing them to propagate in the target's normal direction. This analysis highlights the close relationship between the spatial distribution of hot electrons (Fig. 7) and EMPs (Fig. 2), thus confirming that hot electrons are the primary source of EMPs.

3.5 Investigation into protection for EMPs

Early nuclear detonation experiments revealed that EMPs generated by nuclear explosions traversed the atmosphere, thus adversely affecting the terrestrial power infrastructure, electronic systems, and human personnel. This is due to the unique physical repercussions induced by the microwave irradiation of materials, including molecular heating, which can cause injury to biological cellular tissues. The coupling of microwaves with electronic systems engenders electromagnetic induction effects, thus resulting in disruptions to electronic equipment. Correspondingly, investigations into laser-driven nuclear fusion reactions and related applications showed that the coupling of lasers with targets results in high-intensity broadband EMPs. These EMPs not only cause severe perturbations in diagnostic data (even potentially submerging test signals entirely amidst electromagnetic interference) but also propagate electromagnetic disturbances onto the diagnostic apparatus both inside and outside the target chamber. This can result in the impairment of precision instruments and pose varying degrees of harm to a person present in environments characterized by robust electromagnetic fields.

Researchers have implemented shielding measures, such as using lead and concrete at Lawrence Livermore National Laboratory [47], as well as employing metallic or iron oxide materials to create Faraday cages integrated with suitable grounding at the National Ignition Facility [17, 48]. At China's Laser Fusion Research Center [49], researchers have investigated the shielding effectiveness of materials such as copper, lead, and copper meshes against EMPs. Building upon these efforts to mitigate EMP interference, we investigate the effectiveness of composite shielding materials in attenuating EMPs by focusing on copper + permalloy + lead composites of various thicknesses. Copper is selected owing to its excellent conductivity, whereas permalloy is selected for its high permeability, both of which contribute significantly to the shielding effect against electromagnetic fields. Meanwhile, lead is incorporated into the composite material for its strong shielding properties against high-energy radiation and neutrons, which reduces the generation of secondary electrons caused by their interaction with the metal, thereby reducing EMP radiation from the electron source. Therefore, this composite shielding material possesses comprehensive ability to shield against electric/magnetic fields as well as secondary electromagnetic fields caused by high-energy radiation, thus rendering it highly advantageous for certain applications.

To evaluate the spatial distribution of the EMP outside the target, we selected three representative locations: a7, a9, and a10. Figure 8a shows the peak attenuation of the EMP passing through the target chamber for glass flanges, metal flanges, and spaces outside the target. Attenuation was quantified by calculating the ratio of the peak values of a5 to those of a7, a9, and a10. The attenuation ratios for glass flanges, metal flanges, and spaces outside the target were 5.21, 2183.98, and 136.81, respectively. This suggests that metal flanges and long-distance transmission can cause significant EMP attenuation, thus facilitating shielding, particularly through the increased utilization of metal flanges and the positioning of shielded equipment at greater distances from the glass flanges. Figure 8b shows the shielding effect of four composite materials (copper + permalloy + lead) with four different thicknesses on EMPs, including 0.05 + 0.3 + 0.6, 0.9 + 0.9 + 0.9, 1.2 + 1.2 + 1.2, and 1.5 + 1.5 + 1.5, in units of micrometer. The shielding effects were 42.8, 290, 339.38, and 540 times, respectively. These results show that the shielding effect of the EMP improved as the thickness of the shielding material increased.

Hu et al. [50] developed a gated fiber detector that was resistant to strong EMP interference by employing optoelectronic isolation. Currently, additional shielding schemes are being actively verified in practical environments. These include the use of photoelectric conversion modules, magnetic rings, surge protectors, absorbing materials, and effective grounding techniques, all of which aim to mitigate the effects of strong EMPs. We plan to develop more comprehensive shielding solutions, which are anticipated to not only extend the service life of the equipment but also enhance electromagnetic compatibility.

4 Conclusion

In this study, we analyzed and compared the characteristics of EMPs generated by the interaction between a powerful fs laser and various targets, including metal,

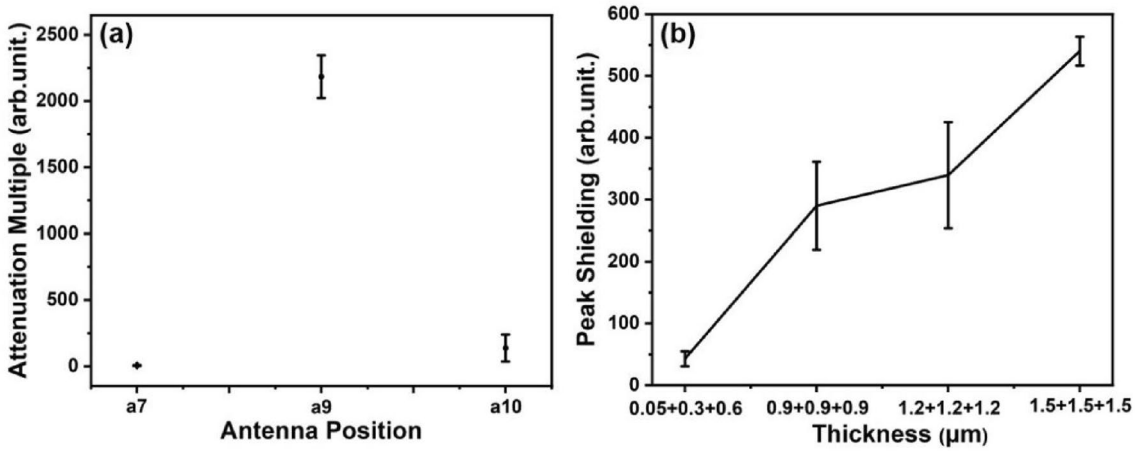

Fig. 8 **a** Spatial distribution of EMP outside target chamber; attenuation multiples of a7, a9, and a10 with respect to peaks of a5. **b** Shielding effect of composites (copper + permalloy + lead) with different thicknesses on EMP peak strength. Thicknesses include 0.05 + 0.3 + 0.6, 0.9 + 0.9 + 0.9, 1.2 + 1.2 + 1.2, and 1.5 + 1.5 + 1.5, in units of micrometer, and peak shielding was obtained by dividing the peak of a7 by that of a8. a5 is located closest to the propagation direction of laser. a7 is located on the glass flange outside target chamber and near exterior of shielding box. a8 is located inside shielding box. a9 is positioned on metal flange. 10 is located 3.8 m away from target chamber wall

plastic flat, and plastic NWA targets. The analysis was performed based on four aspects: spatial distribution, time domain, frequency domain, and radiation energy. Our findings revealed that EMPs in the target chamber were dispersed at different angles, with higher strength observed for metal targets than for plastic targets. Hence, the electronic devices located in front of and behind the target chamber required protection. In addition, the EMP strength was higher near the glass flange outside the target chamber, thus emphasizing the necessity to shield the electronic devices in this area. Moreover, adjusting the laser focal spot, target holder, and target parameters enabled the generation of EMPs with different energies and frequencies. These EMPs can be used to suppress, enhance, or control EMPs, as well as be used as specialized broadband high-energy microwave sources. This study highlighted the significance of electromagnetic protection in high-power laser facilities, particularly when using metallic targets. The use of composite shielding materials was shown to be effective in shielding EMPs. Further research will be conducted on this topic, e.g., comparing the usefulness of different composite and single materials. In summary, the results of this study are valuable for investigating the characteristics of EMPs generated by laser-matter interactions and for protecting electronic equipment from electromagnetic interference. These topics shall be further investigated in future studies.

Author contributions All authors contributed to the study conception and design. Material preparation, data collection and analysis were performed by YDX, DFK, QYH, ZG, DJZ, TY, HC, YZL, YY, XL, PZ, XLX, JQZ, TSL, CL, WJM and XQY. The first draft of the manuscript was written by YDX and all authors commented on previous versions of the manuscript. All authors read and approved the final manuscript.

Data and materials availability The data that support the findings of this study are openly available in Science Data Bank at https://cstr.cn/31253.11.sciencedb.j00186.00350 and https://www.doi.org/https://doi.org/10.57760/sciencedb.j00186.00350.

Declarations

Conflict of interest Xue-Qing Yan is an editorial board member for Nuclear Science and Techniques and was not involved in the editorial review, or the decision to publish this article. All authors declare that there are no competing interests.

References

1. C.D. Decker, W.B. Mori, J.M. Dawson, Nonlinear collisional absorption in laser-driven plasmas. Phys. Plasmas **1**, 4043–4049 (1994). https://doi.org/10.1063/1.870874
2. J.P. Freidberg, R.W. Mitchell, R.L. Morse et al., Resonant absorption of laser light by plasma targets. Phys. Rev. Lett. **28**, 795 (1972). https://doi.org/10.1103/PhysRevLett.28.795
3. F. Brunel, Not-so-resonant, resonant absorption. Phys. Rev. Lett. **59**, 52 (1987). https://doi.org/10.1103/PhysRevLett.59.52
4. W.L. Kruer, Kent Estabrook, J×B heating by very intense laser light. Phys. Fluids **28**, 430–432 (1985). https://doi.org/10.1063/1.865171
5. T. Tajima, J.M. Dawson, Laser electron accelerator. Phys. Rev. Lett. **43**(4), 267 (1979). https://doi.org/10.1103/PhysRevLett.43.267
6. M. Tabak, J. Hammer, M.E. Glinsky et al., Ignition and high gain with ultrapowerful lasers. Phys. Plasmas **1**(5), 1626 (1994). https://doi.org/10.1063/1.870664
7. M.H. Key, E.M. Campbell, T.E. Cowan et al., The potential of fast ignition and related experiments with a petawatt laser facility. J.

Fusion Energy **17**(3), 231 (1998). https://doi.org/10.1023/A:1021862430021
8. P.G. O'Shea, H.P. Freund, Free-electron lasers: status and applications. Science **292**, 1853 (2001). https://doi.org/10.1126/science.1055718
9. S. Singh, C.D. Armstrong, N. Kang et al., Bremsstrahlung emission and plasma characterization driven by moderately relativistic laser–plasma interactions. Plasma Phys. Control. Fusion **63**(3), 035004 (2020). https://doi.org/10.1088/1361-6587/abcf7e
10. H.Y. Lan, D. Wu, J.X. Liu et al., Photonuclear production of nuclear isomers using bremsstrahlung induced by laser-wakefield electrons. Nucl. Sci. Tech. **34**(5), 74 (2023). https://doi.org/10.1007/s41365-023-01219-x
11. Z. Cao, W. Qi, H. Lan et al., Experimental study of medical isotopes ^{62,64}Cu and ^{68}Ga production using intense picosecond laser pulse. Plasma Phys. Control. Fusion **65**(5), 055007 (2023). https://doi.org/10.1088/1361-6587/acc090
12. J.W. Yang, T.S. Li, T. Yi et al., Measurement and analysis of electromagnetic pulse from laser-target interaction at ShenGuang II laser facility. Fusion Sci. Technol. **72**, 41 (2017). https://doi.org/10.1080/15361055.2016.1273690
13. M. Yang, Y. Yang, T. Li et al., Electromagnetic radiations from laser interaction with gas-filled Hohlraum. Laser Phys. Lett. **15**, 016101 (2017). https://doi.org/10.1088/1612-202X/aa94ec
14. F. Consoli, P.L. Andreoli, M. Cipriani et al., Sources and space–time distribution of the electromagnetic pulses in experiments on inertial confinement fusion and laser–plasma acceleration. Philos. T. R. Soc. A **379**, 20200022 (2021). https://doi.org/10.1098/rsta.2020.0022
15. T. Nakamura, S. Kato, H. Nagatomo et al., Surface-magnetic-field and fast-electron current-layer formation by ultraintense laser irradiation. Phys. Rev. Lett. **93**, 265002 (2004). https://doi.org/10.1103/PhysRevLett.93.265002
16. C.C. Cheng, E.M. Wright, J.V. Moloney, Generation of electromagnetic pulses from plasma channels induced by femtosecond light strings. Phys. Rev. Lett. **87**, 213001 (2001). https://doi.org/10.1103/PhysRevLett.87.213001
17. D.C. Eder, A. Throop, C.G. Brown et al., Mitigation of electromagnetic pulse (EMP) effects from short-pulse lasers and fusion neutrons. Lawrence Livermore National Laboratory LLNL-TR-411183, (2009). https://doi.org/10.2172/950076
18. J.L. Dubois, F. Lubrano-Lavaderci, D. Raffestin et al., Target charging in short-pulse-laser-plasma experiments. Phys. Rev. E **89**, 013102 (2014). https://doi.org/10.1103/PhysRevE.89.013102
19. A. Poye, J.L. Dubois, F. Lubrano-Lavaderci et al., Dynamic model of target charging by short laser pulse interactions. Phys. Rev. E **92**, 043107 (2015). https://doi.org/10.1103/PhysRevE.92.043107
20. A. Poyé, S. Hulin, M. Bailly-Grandvaux et al., Physics of giant electromagnetic pulse generation in short-pulse laser experiments. Phys. Rev. E **91**, 043106 (2015). https://doi.org/10.1103/PhysRevE.91.043106
21. H. Jin, C. Meng, Y. Jiang et al., Simulation of electromagnetic pulses generated by escaped electrons in a high-power laser chamber. Plasma Sci. Technol. **20**, 115201 (2018). https://doi.org/10.1088/2058-6272/aac838
22. M.D. Marco, J. Cikhardt, J. Krása et al., Electromagnetic pulses produced by expanding laser-produced Au plasma. Nukleonika **60**, 239–243 (2015). https://doi.org/10.1515/nuka-2015-0043
23. S. Varma, J. Spicer, B. Brawley et al., Plasma enhancement of femtosecond laser-induced electromagnetic pulses at metal and dielectric surfaces. Opt. Eng. **53**, 051515 (2014). https://doi.org/10.1117/1.OE.53.5.051515
24. P. Bradford, N.C. Woolsey, G.G. Scott et al., EMP control and characterization on high-power laser systems. High Power Laser Sci. Eng. **6**, e21 (2018). https://doi.org/10.1017/hpl.2018.21
25. K. Nelissen, M. Liszi, M.D. Marco et al., Characterisation and modelling of ultrashort laser-driven electromagnetic pulses. Sci. Rep. **10**, 3108 (2020). https://doi.org/10.1038/s41598-020-59882-8
26. C.G. Brown Jr., E. Bond, T. Clancy et al., Assessment and mitigation of electromagnetic pulse (EMP) impacts at short-pulse laser facilities. J. Phys. Conf. Ser. **244**, 032001 (2010). https://doi.org/10.1088/1742-6596/244/3/032001
27. Y. Xia, D. Li, S. Zhang et al., Enhancing electromagnetic radiations by a pre-ablation laser during laser interaction with solid target. Phys. Plasmas **27**, 032705 (2020). https://doi.org/10.1063/1.5140585
28. C.N. Danson, C. Haefner, J. Bromage et al., Petawatt and exawatt class lasers worldwide. High Power Laser Sci. Eng. **7**, 54 (2019). https://doi.org/10.1017/hpl.2019.36
29. G. Mourou, Nobel lecture: extreme light physics and application. Rev. Mod. Phys. **91**(3), 030501 (2019). https://doi.org/10.1103/RevModPhys.91.030501
30. F. Consoli, V.T. Tikhonchuk, M. Bardon et al., Laser produced electromagnetic pulses: generation, detection and mitigation. High Power Laser Sci. Eng. **8**, e22 (2020). https://doi.org/10.1017/hpl.2020.13
31. X. Xie, J. Zhu, Q. Yang et al., Multi petawatt laser design for the ShenGuang II laser facility. High-Power High-Energy High-Intensity Laser Technol. II **9513**, 95130A (2015). https://doi.org/10.1117/12.2178621
32. J. Zhu, X. Xie, M. Sun et al., Analysis and construction status of SG-II 5PW laser facility. High Power Laser Sci. Eng **6**, e29 (2018). https://doi.org/10.1017/hpl.2018.23
33. M. Yang, T.S. Li, C. Wang et al., Characterization of electromagnetic pulses via arrays on ShenGuang-III laser facility laser. Chinese Opt. Lett. **14**, 101402 (2016). https://doi.org/10.3788/COL201614.101402
34. X.Z. Wu, Z. Gong, Y.R. Shou et al., Efficiency enhancement of ion acceleration from thin target irradiated by multi-PW few-cycle laser pulses. Phys. Plasmas **28**, 023102 (2021). https://doi.org/10.1063/5.0029171
35. E. Eftekhari-Zadeh, M.S. Blümcke, Z. Samsonova et al., Laser energy absorption and X-ray generation in nanowire arrays irradiated by relativistically intense ultra-high contrast femtosecond laser pulses. Phys. Plasmas **29**, 013301 (2022). https://doi.org/10.1063/5.0064364
36. R. Xie, L.H. Cao, Y. Chao et al., Improvement of laser absorption and control of particle acceleration by subwavelength nanowire target. Phys. Plasmas **27**, 123108 (2020). https://doi.org/10.1063/5.0022144
37. Y. Shou, D. Kong, P. Wang et al., High-efficiency water-window X-ray generation from nanowire array targets irradiated with femtosecond laser pulses. Opt. Express **29**(4), 5427–5436 (2021). https://doi.org/10.1364/OE.417512
38. D. Kong, G. Zhang, Y. Shou et al., High-energy-density plasma in femtosecond-laser-irradiated nanowire-array targets for nuclear reactions. Matter Radiat. Extremes **7**, 064403 (2022). https://doi.org/10.1063/5.0120845
39. Y. Xia, F. Zhang, H. Cai et al., Analysis of electromagnetic pulses generation from laser coupling with polymer targets: effect of metal content in target. Matter Radiat. Extremes **5**, 017401 (2020). https://doi.org/10.1063/1.5114663
40. M.D. Marco, M. Pfeifer, E. Krousky et al., Basic features of electromagnetic pulse generated in a laser-target chamber at 3-TW laser facility PALS. J. Phys. Conf. Ser. **508**, 012007 (2014). https://doi.org/10.1088/1742-6596/508/1/012007
41. M.J. Mead, D. Neely, J. Gauoin et al., Electromagnetic pulse generation within a petawatt laser target chamber. Rev. Sci. Instrum. **75**, 4225 (2004). https://doi.org/10.1063/1.1787606

42. F. Consoli, R.D. Angelis, M.D. Marco et al., EMP characterization at PALS on solid-target experiments. Plasma Phys. Control. Fusion **60**, 105006 (2018). https://doi.org/10.1088/1361-6587/aad709
43. K.V. Lezhnin, F.F. Kamenets, T.Z. Esirkepov et al., Laser ion acceleration from mass-limited targets with preplasma. Phys. Plasmas **23**(5), 053114 (2016). https://doi.org/10.1063/1.4950836
44. S.C. Wilks, A.B. Langdon, T.E. Cowan et al., Energetic proton generation in ultra-intense laser–solid interactions. Phys. Plasmas **8**, 542 (2001). https://doi.org/10.1063/1.1333697
45. S. Jiang, A.G. Krygier, D.W. Schumacher et al., Effects of front-surface target structures on properties of relativistic laser-plasma electrons. Phys. Rev. E **89**, 013106 (2014). https://doi.org/10.1103/PhysRevE.89.013106
46. S. Jiang, L.L. Ji, H. Audesirk et al., Microengineering laser plasma interactions at relativistic intensities. Phys. Rev. Lett. **116**, 085002 (2016). https://doi.org/10.1103/PhysRevLett.116.085002
47. C. Stoeckl, V.Y. Glebov, P.A. Jaanimagi et al., Operation of target diagnostics in a petawatt laser environment (invited). Rev. Sci. Instrum. **77**, 10F506 (2006). https://doi.org/10.1063/1.2217922
48. J.R. Kimbrough, P.M. Bell, G.B. Christianson et al., National ignition facility core X-ray streak camera. Rev. Sci. Instrum. **72**, 748–750 (2001). https://doi.org/10.1063/1.1318262
49. L. Zhao, T. Li, Y. Xia et al., Effective electromagnetic shielding with multi-layer structure material on shenguang laser facility. Plasma Sci. Technol. **22**(2), 025601 (2019). https://doi.org/10.1088/2058-6272/ab5068
50. P. Hu, Z.G. Ma, K. Zhao et al., Development of gated fiber detectors for laser-induced strong electromagnetic pulse environments. Nucl. Sci. Tech. **32**(6), 58 (2021). https://doi.org/10.1007/s41365-021-00898-8

Springer Nature or its licensor (e.g. a society or other partner) holds exclusive rights to this article under a publishing agreement with the author(s) or other rightsholder(s); author self-archiving of the accepted manuscript version of this article is solely governed by the terms of such publishing agreement and applicable law.